Title: Spectroscopic observation of resonances in the $F+H_2$ reaction

Authors: Jongjin B. Kim[1]†, Marissa L. Weichman[1], Tobias F. Sjolander[1], Daniel M. Neumark[1,2]*, Jacek Klos[3], Millard H. Alexander[3,4]*, David E. Manolopoulos[5]*.

Affiliations:

[1]Department of Chemistry, University of California, Berkeley, CA 94720, USA.

[2]Chemical Sciences Division, Lawrence Berkeley National Laboratory, Berkeley, CA 94720, USA.

[3]Department of Chemistry and Biochemistry, University of Maryland, College Park, MD 20742, USA.

[4] Institute for Physical Science and Technology, University of Maryland, College Park, MD 20742

[5] Department of Chemistry, Oxford University, Physical and Theoretical Chemistry Laboratory, South Parks Road, Oxford, OX1 3QZ, UK.

*Correspondence to: dneumark@berkeley.edu (D.M.N.); mha@umd.edu (M.H.A.); david.manolopoulos@chem.ox.ac.uk (D.E.M.)

†Current address: SLAC National Accelerator Laboratory, Menlo Park, CA 94025, USA

One Sentence Summary:

High-resolution photoelectron spectroscopy provides a definitive observation of the elusive resonances in the benchmark $F+H_2$ reaction.

Abstract:

Photodetachment spectroscopy of the FH_2^- and FD_2^- anions allows for the direct observation of reactive resonances of the benchmark reaction $F + H_2 \rightarrow HF + H$. Using cooled anion precursors and a high-resolution electron spectrometer, we observe several narrow peaks not seen in previous experiments. Theoretical calculations, based on a highly accurate $F+H_2$ potential energy surface, convincingly assign these peaks to resonances associated with quasi-bound states in the HF+H and DF+D product arrangements, and with a quasi-bound state in the transition state region of the $F+H_2$ reaction. The calculations also reveal quasi-bound states in the reactant arrangement, which have yet to be resolved experimentally.

Main Text:

Much of our understanding of the structures of stable molecules has come from spectroscopy. The analysis of bound-bound transitions yields molecular geometries and frequencies – the molecular potential energy surface. The observation of similar sharp structures during a chemical reaction would give comparable insight into the reactive potential energy surface, in particular for the all-important transition state region (*1*). The fleeting nature of the transition state makes this task much more challenging, however. Here, we report the spectroscopic observation of sharp resonance structures associated with the transition state and product valley regions of the $F+H_2 \rightarrow HF+H$ reaction, a benchmark reaction in the field of chemical reaction dynamics (*2*).

The rapid variation of a scattering cross section with energy or angle has long guided physicists in the investigation of nuclear and sub-nuclear structure. These so-called "resonances" are signs of metastable excited states or previously unknown particles. In chemistry, the experimental and theoretical search for these quantum features in reactive scattering experiments has been intense (*3*-*7*). Although tentative experimental evidence for resonances in the $F+H_2$ reaction was first reported in the 1980s (*8*), it took until 2000 for a resonance to be unambiguously identified in a crossed molecular beam experiment, as a step-like feature in the energy-dependence of the integral cross section of $F+HD \rightarrow HF+D$ (*9, 10*). The same resonance – a quasi-bound state in the FHD transition state region with three quanta of excitation in the H–F stretch and none in either the H–D stretch or the bend – has since been found under higher resolution to give rise to undulations in individual state-to-state differential cross sections of the reaction as a function of the collision energy (*11*). More recent molecular beam experiments combined with theoretical simulations have also provided some evidence for a resonance (*12*) (or perhaps two resonances (*13*)) in the reaction of the $F+H_2$ isotopologues.

Anion photoelectron spectroscopy provides an alternative experimental approach to the study of chemical reactions (*14*). Because the geometry of the FH_2^- anion is close to that of the neutral $F+H_2$ transition state, photodetachment of the electron from the anion provides a direct spectroscopic probe of the transition state dynamics (*15*), as illustrated in Figure 1. If the precursor anion is rotationally cold, this probe avoids the averaging over angular momentum that tends to obscure resonances in a crossed molecular beam experiment. Previous spectra of FH_2^- have revealed broad peaks associated with the bending levels of the FH_2 transition state complex, which correspond to the "quantized bottlenecks" of the reaction rather than reactive scattering resonances (*16*). Calculations based on the best potential energy surface then available reproduced the positions and intensities of these broad peaks, as well as predicting a number of

narrower peaks, which were assigned to resonances (*17*). Unfortunately, the experimental resolution available at the time (~20 meV) was not high enough to permit the detection of these features.

The development of slow-electron velocity-map imaging (SEVI) with cryogenic ion cooling has enabled the acquisition of photoelectron spectra of complex species with sub-meV resolution (*18*). Much improved signal-to-noise compared to a previous SEVI report (*19*) has allowed the detection of sharp peaks in the spectra of both FH_2^- and FD_2^-, which we report here.

The experimental apparatus has been described in detail previously (*18, 20*), with relevant features highlighted in the Supplementary Material (*21*). The FH_2^- and FD_2^- ions are created by introducing F^- anions into a cryogenically cooled ion trap containing H_2 or D_2 buffer gas at low pressure; the resulting ion yield is substantially higher than in previous work where FH_2^- was generated in a molecular beam ion source. The ions are extracted from the trap, mass-selected, and photodetached at various photon energies. The photoelectron kinetic energy (E_{ke}) distribution is obtained with SEVI, in which a velocity-map imaging electron spectrometer (*22*) operated at comparatively low extraction voltages produces high-resolution (sub-meV) photoelectron spectra at low E_{ke}. The electron binding energy (E_{be}) gives the energy difference between the anion and neutral states, and is obtained by subtracting the measured E_{ke} from the photon energy. As previous simulations suggested more obvious signatures of resonances with *para*-H_2 than *ortho*-H_2 (*17*), the FH_2^- ions were enriched in *p*-H_2. However, the FD_2^- ions were formed by trapping F^- in a buffer gas of *normal* deuterium (*n*-D_2).

Several earlier publications outline the calculation of the photodetachment spectrum of the FH_2^- anion (*17, 23*). Photodetachment projects the vibrational wave function of the anion onto the F+H_2 potential energy surface, where it evolves under the influence of the neutral FH_2 Hamiltonian. In the Condon approximation, the photodetachment spectrum *P(E)* is the Fourier transform of the overlap between this evolving wave function and the initial anion vibrational wave function (*17*). We use here the very high quality LWAL F+H_2 potential energy surface (*24*), which is based on multi-reference, configuration-interaction calculations. The relation between the experimental binding energy (E_{be}) and the energy E in the theoretical simulation, which refers to the bottom of the F+H_2 reactant valley with the F atom in its ground ($^2P_{3/2}$) spin-orbit state, is

$$E_{be} = E - ZPE(H_2) + EA(F) + D_0(FH_2^-), \quad (1)$$

where *ZPE* is the zero-point energy of H_2, *EA* is the electron affinity of F, and D_0 is the dissociation energy of the FH_2^- anion. These energetics are illustrated schematically in Fig. 1. In

the theoretical simulations we use the experimental *EA* of F [3.4012 eV (*25*)] and the *ZPE*'s for H_2 and D_2 as predicted by the LWAL PES (0.2705 eV and 0.1918 eV respectively). To determine D_0 we have performed new *ab initio* and vibrational bound state calculations described in the Supplementary Material, obtaining D_0 = 0.2005 eV for FH_2^- and 0.2219 eV for FD_2^-.

The experimental and simulated SEVI spectra of *p*-FH_2^- and *n*-FD_2^- are presented in Figures 2 and 3, respectively. Spectra at additional photon energies are shown in Figs. S1 and S2. Figures S3 and S4 show a comparison of the *p*-FH_2^- photodetachment spectra predicted by two different antion wavefunctions (Fig. S3) and by two different potential energy surfaces (Fig. S4). The overview *p*-FH_2^- photodetachment spectrum is dominated by three broad peaks, labeled *A*, *B* and *C* in Fig. 2. These had been previously assigned to hindered H_2 rotor (or bending) states of the transient FH_2 complex (*16, 26*). The equilibrium geometry of the linear FH_2^- anion is just on the reactant side of the neutral transition state. Because the minimum F+H_2 barrier on the neutral potential energy surface has a bent geometry, photodetachment of the electron excites a bending progression in the neutral FH_2 complex. We also observe a smaller peak in the high resolution *p*-FH_2^- spectrum, labeled *a*, just above the first broad peak *A*. This peak has not been resolved in any previous experiment. It also occurs in the simulated spectra, along with two smaller peaks (labeled β and γ) at higher energy, and a pronounced peak (labeled α, seen experimentally as a slight shoulder) on the low-energy side of peak *A*.

The situation for *n*-FD_2^- is similar. The experimental overview spectrum in Fig. 3 is dominated by two broad peaks, labeled *D* and *E*. The high-resolution spectrum shows two smaller peaks to lower energy, labeled *b* and *c*. These smaller peaks are also seen in the theoretical spectra, along with an additional small peak labeled δ, which is not resolved in the experimental spectrum. In both cases (*p*-FH_2^- and *n*-FD_2^-), the agreement between the positions of the calculated and the observed high-resolution peaks (peak *a* in Fig. 2 and peaks *b* and *c* in Fig. 3) is excellent, suggesting that an analysis of the theoretical calculations will provide a reliable guide to the origin of these experimental peaks. What makes this comparison especially compelling is that no arbitrary shift was introduced to align the experimental and theoretical spectra in Figs. 2 and 3; use of the *ab initio* values of D_0 for FH_2^- and FD_2^- in the relationship between E and E_{be} in eq. 1 positions the theoretical spectra.

Calculating the scattering wave function $\psi(E)$ at the energy E of each peak allows us to characterize the peaks in the theoretical spectra in Figs. 2 and 3. This is the same procedure used previously by Russell and Manolopoulos (*17*). The details of the present, more accurate calculations of the wave functions $\psi(E)$ are given in the Supplementary Material (*21*).

Figure 4 shows plots of the wave functions corresponding to the low-energy resonance peaks α, *A*, and *a* in Fig. 2, and peaks *b*, *c*, and δ in Fig. 3, in collinear F–H–H (F–D–D) geometry. This figure unambiguously elucidates the nature of the peaks in the photodetachment spectra: peaks α and δ are reactant resonances, peak *A* is a transition state resonance, and peaks *a*, *b*, and *c* are product resonances. The quasi-bound states that give rise to these resonances are localized in the reactant F+H_2 (F+D_2) van der Waals well, the FH_2 transition state, and the product HF+H (DF+D) van der Waals well, respectively. The green contours in Fig. 4 depict the anion wavefunctions. Figure S6 illustrates the position of the FH–H and FD–D product state resonances with an adiabatic-bender model. (*27-29*)

It is possible to assign quantum numbers to the resonance wave functions based on their nodal structure. The reactant resonances have quantum numbers *v*, *j*, and *t*, where *v* enumerates the number of quanta in the H–H stretch, *j* in the hindered H_2 rotation, and *t* in the F–H_2 stretch of the F+H_2 van der Waals complex. For the product resonances v′, *j′*, and *t′,* refer, similarly, to the H–F stretch, the hindered HF rotation, and the H–HF van der Waals stretch. The quantum numbers of the reactant resonances in Fig. 4 are (v,*j*,*t*) = (0,0,0) for both α (*p*-FH_2^-) and δ (*n*-FD_2^-), whereas the quantum numbers of the product resonances are (v′,*j′*,*t′*) = (3,0,0) for *a*, and (v′,*j′*,*t′*) = (4,0,0) and (4,0,1) for *b* and *c*, respectively. Finally, the transition state resonance that gives rise to peak *A* in the *p*-FH_2^- spectrum has three quanta in the H–F stretch (ν_1), and none in either the F–H–H bend (ν_2) or the H–H stretch (ν_3).

The resonances *a*, *b*, and *c* that have been detected as narrow peaks in the present high-resolution SEVI spectra of *p*-FH_2^- and *n*-FD_2^- are thus all product resonances: quasi-bound states localized in the van der Waals well region in the product valley. Because the energies of these resonances are below the thresholds for production of HF(v′=3)+H and DF(v′=4)+D, they cannot decay into these channels, and must decay instead into HF(v′=2)+H and DF(v′=3)+D by vibrational predissociation (the hallmark of a Feshbach resonance). The reason why there are two resonances for FD_2 and only one for FH_2 can be traced to the larger mass of D, which leads to two quasi-bound states in the D–DF(v′=4,*j′*=0) van der Waals stretching coordinate rather than just one (see the Supplementary Material for a more detailed analysis). The emergence of peak *a* at high resolution was predicted by Russell and Manolopoulos in their earlier theoretical study of the *p*-FH_2^- spectrum (*17*), but peaks *b* and *c* in the *n*-FD_2^- spectrum have been neither predicted nor measured until now.

The broader low-energy peak *A* in the *p*-FH_2^- spectrum was incorrectly assigned in earlier work to a “direct scattering” or “quantized” state associated with the opening of the F+H_2(v=0,*j*=0) channel at the transition state (*17*). However, it is clear from the present

calculations that the wave function $\psi(E)$ at the energy of this peak is localized in the transition state region rather than delocalized along the reaction coordinate. This localization is the characteristic feature of a resonance wave function (*30*). This resonance has precisely the same form and quantum numbers as the transition state resonance found by Skodje *et al.* in the F+HD reaction (*9, 10*). It is thus simply an analytic continuation of this resonance in the mass of one of the two hydrogen atoms.

All of the other peaks in Figs. 2 and 3 can be assigned in the same way by examining the scattering wave functions at the peak energies. The results of these assignments are summarized in Table 1. The broad peaks *B* and *C* in Fig. 2 and *D* and *E* in Fig. 3 are due to quantized bottlenecks associated with the opening of new channels at the transition state, with wave functions that are delocalized along the reaction coordinate (*30*); the associated wavefunctions are shown in Fig. S5. The narrow peaks β and γ in Fig. 2 are reactant resonances with quantum numbers (v,*j,t*) = (0,2,0) and (0,4,0), respectively. Like peak δ in Fig. 3, the theoretical calculations predict only low intensity for these peaks. They have yet to be resolved experimentally. As shown in Fig. S4, the agreement between the experimental and theoretical resonance positions is noticeably poorer using another recently developed F + H_2 surface (*31*), illustrating that the resonances are indeed a sensitive and experimentally accessible probe of the neutral reactive surface.

We have shown that high resolution SEVI photodetachment spectra of *p*-FH_2^- and *n*-FD_2^- anions reveal previously unresolved peaks in the low-energy region that can unambiguously be attributed to reactive scattering resonances. The signatures of these resonances in the SEVI spectra are far clearer than they would be in a crossed molecular beam experiment, where angular momentum averaging washes out resonance features in both integral and differential cross sections. Thanks to recent experimental developments (including SEVI and, crucially for the present study, the use of a cryogenically cooled ion trap to produce large amounts of *p*-FH_2^- and *n*-FD_2^-), high resolution anion photodetachment spectroscopy does indeed provide an effective way to observe the elusive resonances in F+H_2 reactive scattering, as was predicted by Russell and Manolopoulos almost 20 years ago (*17*).

References and Notes:

1. J. C. Polanyi, A. H. Zewail, *Acc. Chem. Res.* **28**, 119 (1995).
2. D. E. Manolopoulos, *J. Chem. Soc. Faraday Trans.* **93**, 673 (1997).

3. G. C. Schatz, *Science* **288**, 1599 (2000).

4. F. Fernández-Alonso, R. N. Zare, *Annu. Rev. Phys. Chem.* **53**, 67 (2002).

5. X. Yang, D. H. Zhang, *Acc. Chem. Res.* **41**, 981 (2008).

6. R. T. Skodje, in *Advances in Quantum Chemistry* C. A. Nicolaides, E. J. Brändas, R. S. John, Eds. (Academic Press, 2012), vol. 63, pp. 119-163.

7. K. Liu, in *Advances in Chemical Physics* S. A. Rice, A. R. Dinner, Eds. (Wiley, Hoboken, NJ, 2012), vol. 149, pp. 1-46.

8. D. M. Neumark, A. M. Wodtke, G. N. Robinson, C. C. Hayden, Y. T. Lee, *J. Chem. Phys.* **82**, 3045 (1985).

9. R. T. Skodje *et al.*, *J. Chem. Phys.* **112**, 4536 (2000).

10. R. T. Skodje *et al.*, *Phys. Rev. Lett.* **85**, 1206 (2000).

11. W. Dong *et al.*, *Science* **327**, 1501 (2010).

12. T. Wang *et al.*, *J. Phys. Chem. Lett.* **5**, 3049 (2014).

13. M. Qiu *et al.*, *Science* **311**, 1440 (2006).

14. D. M. Neumark, *Phys. Chem. Chem. Phys.* **7**, 433 (2005).

15. I. M. Waller, T. N. Kitsopoulos, D. M. Neumark, *J. Phys. Chem.* **94**, 2240 (1990).

16. D. E. Manolopoulos *et al.*, *Science* **262**, 1852 (1993).

17. C. L. Russell, D. E. Manolopoulos, *Chem. Phys. Lett.* **256**, 465 (1996).

18. C. Hock, J. B. Kim, M. L. Weichman, T. I. Yacovitch, D. M. Neumark, *J. Chem. Phys.* **137**, 244201 (2012).

19. T. I. Yacovitch *et al.*, *Faraday Disc.* **157**, 399 (2012).

20. A. Osterwalder, M. J. Nee, J. Zhou, D. M. Neumark, *J. Chem. Phys.* **121**, 6317 (2004).

21. Methods are detailed in Supporting Online Material at Science Online. .

22. A. T. J. B. Eppink, D. H. Parker, *Rev. Sci. Instrum.* **68**, 3477 (1997).

23. J. Z. H. Zhang, W. H. Miller, *J. Chem. Phys.* **92**, 1811 (1990).

24. F. Lique, G. L. Li, H.-J. Werner, M. H. Alexander, *J. Chem. Phys.* **134**, 231101 (2011).

25. C. Blondel, C. Delsart, F. Goldfarb, *J. Phys. B: At. Mol. Opt. Phys.* **34**, 2757 (2001).

26. S. E. Bradforth, D. W. Arnold, D. M. Neumark, D. E. Manolopoulos, *J. Chem. Phys.* **99**, 6345 (1993).

27. S. L. Holmgren, M. Waldman, W. Klemperer, *J. Chem. Phys.* **67**, 4414 (1977).

28. M. H. Alexander, S. Gregurick, P. J. Dagdigian, *J. Chem. Phys.* **101**, 2887 (1994).

29. J. F. Castillo, D. E. Manolopoulos, K. Stark, H.-J. Werner, *J. Chem. Phys.* **104**, 6531 (1996).

30. D. E. Manolopoulos, *Nature* **419**, 266 (2002).

31. B. Fu, X. Xu, D. H. Zhang, *J. Chem. Phys.* **129**, 011103 (2008).
32. I. V. Koptyug *et al.*, *J. Am. Chem. Soc.* **129**, 5580 (2007).
33. T. A. Grinev, A. A. Buchachenko, R. V. Krems, *ChemPhysChem* **8**, 815 (2007).
34. M. B. Doyle, C. Abeyasera, A. G. Suits, *NuACQ,* http://chem.wayne.edu/suitsgroup/NuAcq.html.
35. B. Dick, *Phys. Chem. Chem. Phys.* **16**, 570 (2014).
36. E. P. Wigner, *Phys. Rev.* **73**, 1002 (1948).
37. A. Weaver, D. M. Neumark, *Faraday Discuss.* **91**, 5 (1991).
38. J. Cooper, R. N. Zare, *J. Chem. Phys.* **48**, 942 (1968).
39. C. Bartels *et al.*, *Science* **323**, 1323 (2009).
40. M. D. Feit, J. A. Fleck, *J. Chem. Phys.* **78**, 301 (1983).
41. D. T. Colbert, W. H. Miller, *J. Chem. Phys.* **96**, 1982 (1992).
42. D. E. Manolopoulos, *J. Chem. Phys.* **117**, 9552 (2002).
43. J. A. Nichols, R. A. Kendall, S. J. Cole, J. Simons, *J. Phys. Chem.* **95**, 1074 (1991).
44. T. B. Adler, G. Knizia, H.-J. Werner, *J. Chem. Phys.* **127**, 221106 (2007).
45. G. Knizia, T. B. Adler, H.-J. Werner, *J. Chem. Phys.* **130**, 054104 (2009).
46. T. H. Dunning, *J. Chem. Phys.* **90**, 1007 (1989).
47. F. Weigend, *Phys. Chem. Chem. Phys.* **4**, 4285 (2002).
48. F. Weigend, A. Kohn, C. Hattig, *J. Chem. Phys.* **116**, 3175 (2002).
49. MOLPRO, version 2012.1, a package of ab initio programs.
50. K. Stark, Ph.D. dissertation, Universität Stuttgart (1996).
51. B. Hartke, H.-J. Werner, *Chem. Phys. Lett.* **280**, 430 (1997).
52. C. X. Xu, D. Q. Xie, D. H. Zhang, *Chinese J. Chem. Phys.* **19**, 96 (2006).
53. G. L. Li, H.-J. Werner, F. Lique, M. H. Alexander, *J. Chem. Phys.* **127**, 174302 (2007).
54. J. Chen, Z. G. Sun, D. H. Zhang, *J. Chem. Phys.* **142**, 024303 (2015).
55. H.-J. Werner, M. Kallay, J. Gauss, *J. Chem. Phys.* **128**, 034305 (2008).
56. S. A. Nizkorodov, W. W. Harper, D. J. Nesbitt, *Faraday Disc.* **113**, 107 (1999).
57. M. H. Alexander, D. E. Manolopoulos, H.-J. Werner, *J. Chem. Phys.* **113**, 11084 (2000).
58. E. Garand, J. Zhou, D. E. Manolopoulos, M. H. Alexander, D. M. Neumark, *Science* **319**, 72 (2008).
59. Z. G. Sun, D. H. Zhang, *Int. J. Quantum Chem.* **115**, 689 (2015).

Acknowledgments: The experimental part of this work is funded by the Air Force Office of Scientific Research (AFOSR) under Grant No. FA9550-12-1-0160 and the Defense University Research Instrumentation Program (DURIP) under Grant No. FA9550-11-1-0330. M.L.W. thanks the National Science Foundation for a graduate research fellowship. The experimental data are available upon request from dneumark@berkeley.edu. M.H.A. is grateful for partial support by the U.S. National Science Foundation under grant CHE-1213332. D.E.M. is funded by the Wolfson Foundation and the Royal Society.

Supplementary Materials:

www.sciencemag.org

Experimental and Theoretical Details, and Additional Theoretical Results

Figs. S1, S2, S3, S4, S5, S6

Tables S1, S2

References (30–59)

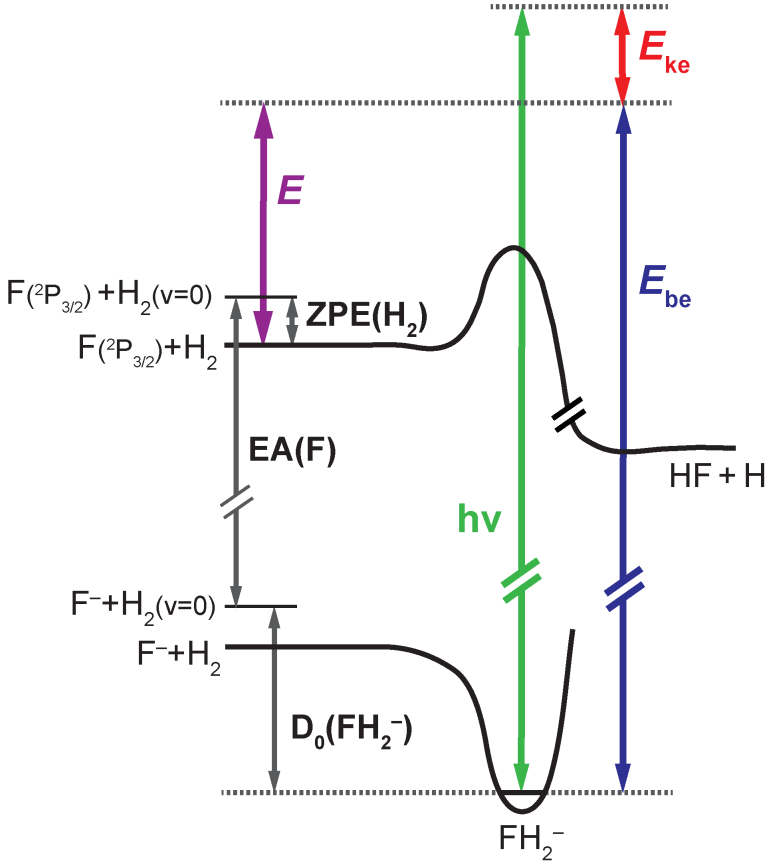

Fig. 1. Schematic of the energetics of the photodetachment process. Arrows show the relationship between the experimental binding energy (E_{be}) and the calculated scattering energy (E).

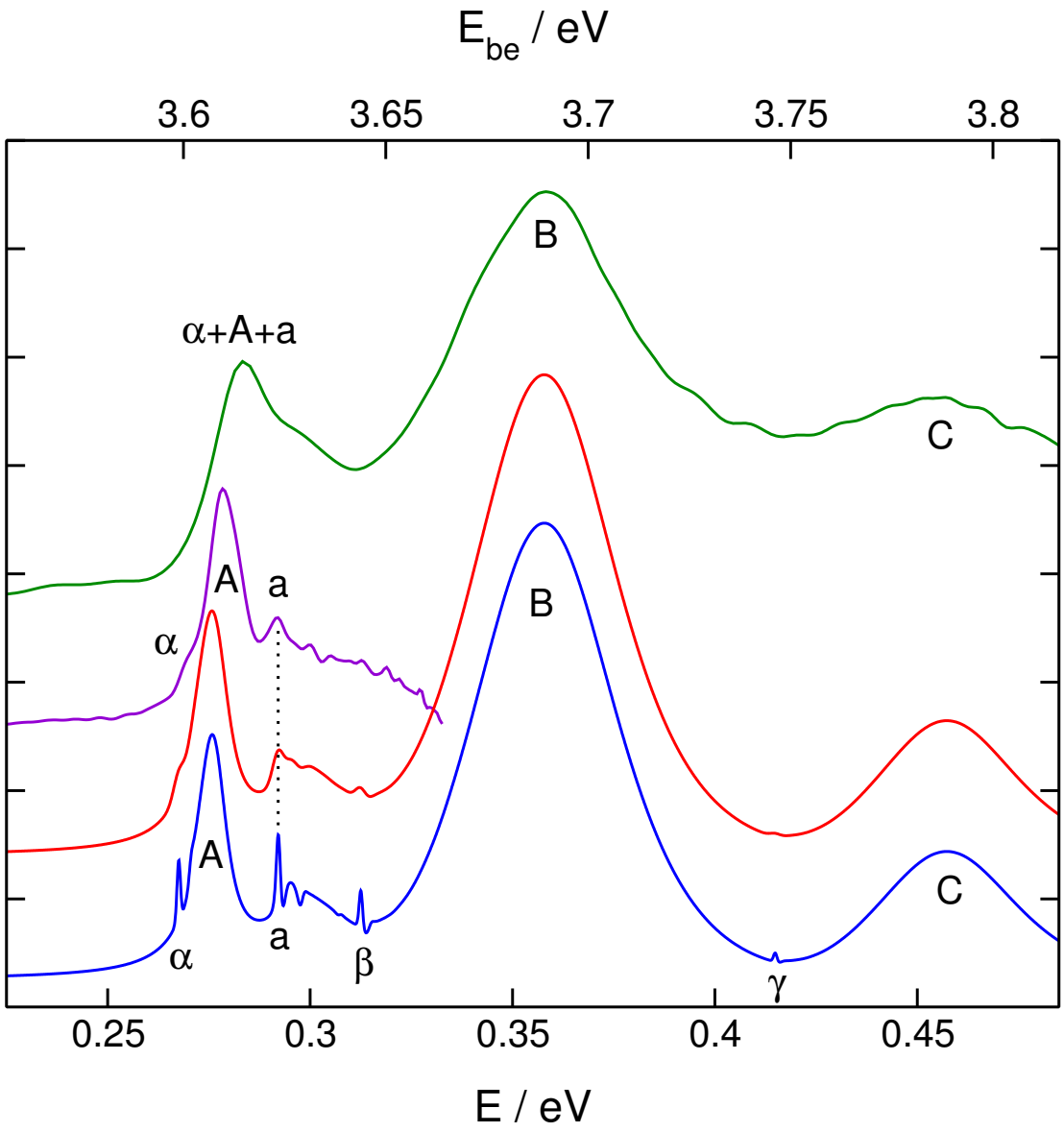

Fig. 2. Photodetachment spectra of *p*-FH_2^-. Green: experimental survey scan (~10 meV resolution). Purple: highest resolution experimental scan (2–3 meV) over a narrower energy window. Blue: theoretical simulation at 1 meV energy resolution. Red: convolution of the theoretical simulation over a Gaussian function with full-width-at-half-maximum (FWHM) of 3 meV. The calculated spectra have not been shifted to match experiment. The relation between the experimental electron binding energy E_{be} and the energy E relative to $F(^2P_{3/2})+H_2(r_e)$ is given by eq. 1 as $E_{be} = E+3.3312$ eV.

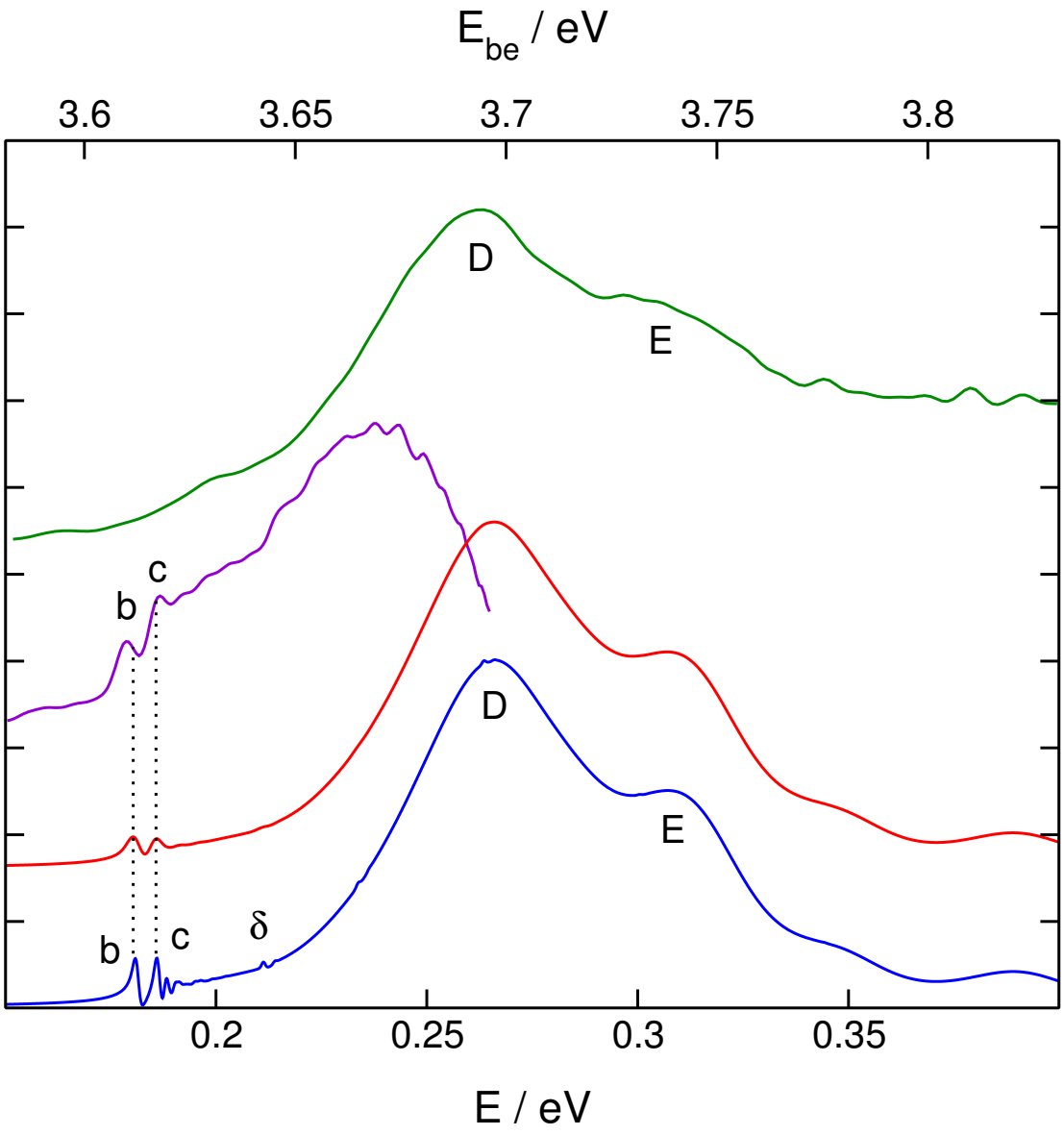

Fig. 3. Photodetachment spectra of *n*-FD_2^-. Green: experimental survey scan (~10 meV resolution). Purple: highest resolution experimental scan (2–3 meV) over a narrower energy window. Blue: theoretical simulation at 1 meV energy resolution. Red: convolution of the theoretical simulation over a Gaussian function with full-width-at-half-maximum (FWHM) of 3 meV. The calculated spectra have not been shifted to match experiment. The relation between the experimental electron binding energy E_{be} and the energy E relative to $F(^2P_{3/2})+H_2(r_e)$ is given by eq. 1 as $E_{be} = E+3.4313$ eV.

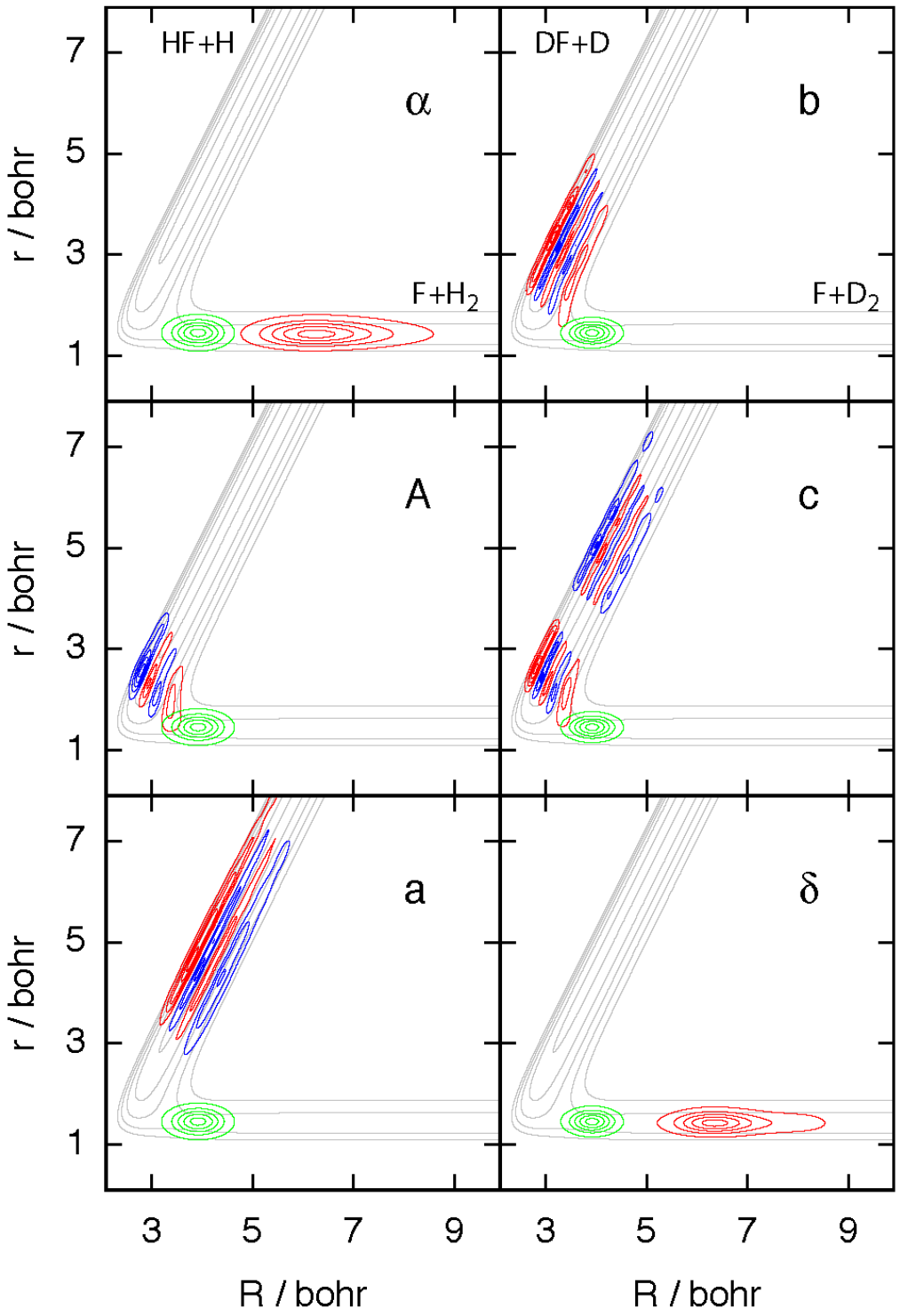
HF+H
α
F+H2
DF+D
b
F+D2
A
c
a
δ
r / bohr
R / bohr
1
3
5
7
9

Fig. 4. Resonance wave functions. The wave functions $\psi(E)$ at the energies E of the first three peaks in the *p*-FH_2^- spectrum in Fig. 2 (α, *A*, and *a*; left), and the first three peaks in the *n*-FD_2^- spectrum in Fig. 3 (*b*, *c*, and δ; right), plotted in collinear geometry, as red ($\psi(E) > 0$) and blue ($\psi(E) < 0$) contours, as a function of the distance R between F and the center-of-mass of H_2 (D_2) and the bond length r of H_2 (D_2). Superimposed in gray are contours of the LWAL potential energy surface *(22)*. Contours of the FH_2^- and FD_2^- anion wave functions are shown in green for comparison. The contoured regions of all wave functions ecompass probability density values greater than than 10% of their maxima; the apparent lack of overlap between the anion wave functions and some of the resonance wave functions arises because the overlap is in the tail (< 10%) of the probability distribution.

Table 1. Assignment of the peaks in the *p*-FH_2^- and *n*-FD_2^- photodetachment spectra in Figs. 2 and 3. The quantum numbers given for the quantized bottlenecks (see Fig. S5) are those of the reactant channel that becomes energetically accessible as a hindered rotor (bending) state at the transition state at the energy of the peak in the photodetachment spectrum.

Spectrum	Peak	E / eV	Assignment	Quantum numbers
p-FH_2^-	α	0.2676	Reactant resonance	$(v,j,t) = (0,0,0)$
	A	0.2758	Transition state resonance	$(\nu_1,\nu_2,\nu_3) = (3,0,0)$
	a	0.2921	Product resonance	$(v',j',t') = (3,0,0)$
	β	0.3125	Reactant resonance	$(v,j,t) = (0,2,0)$
	B	0.3578	Quantized bottleneck	$F+H_2(v=0,j=2)$
	γ	0.4149	Reactant resonance	$(v,j,t) = (0,4,0)$
	C	0.4573	Quantized bottleneck	$F+H_2(v=0,j=4)$
n-FD_2^-	b	0.1809	Product resonance	$(v',j',t') = (4,0,0)$
	c	0.1860	Product resonance	$(v',j',t') = (4,0,1)$
	δ	0.2112	Reactant resonance	$(v,j,t) = (0,0,0)$
	D	0.2661	Quantized bottleneck	$F+D_2(v=0,j=2)$
	E	0.3071	Quantized bottleneck	$F+D_2(v=0,j=4)$

Supplementary Material

Experimental details:

The details of the experimental apparatus have been described in detail previously (*18, 20*). The ions are created, cooled in a cryogenic ion trap, and photodetached at various photon energies. SEVI uses a velocity-map imaging (VMI) electron spectrometer (*22*) at comparatively low extraction voltages, allowing for the acquisition of low-E_{ke}, high-resolution photoelectron spectra with high collection efficiencies.

The most significant differences from our previous report on SEVI spectra of FH_2^- *(19)* are in ion production and cooling, along with image acquisition and processing. Instead of forming FH_2^- ions in a gas jet expansion, they were created in an ion trap. F^- ions were generated by dissociative electron attachment of trace NF_3 in a helium gas expansion. The ions were transferred by ion guides and a quadrupole mass filter to a cryogenic ion trap filled with a burst of hydrogen buffer gas. The H_2/D_2 gas clustered with the fluoride anion and cooled the resulting FH_2^- and FD_2^- complexes, allowing for ion yields several times that in the previous experiment. *p*-H_2 was prepared by flowing *n*-H_2 over an iron oxide catalyst at 30 K (*32*); the spin-isomer-enriched products were stored in an aluminum gas cylinder prior to injection in the ion trap. The expected spin isomer purity is ~95% *p*-H_2.

Temperatures in the ion trap depended on the system of interest. The ion trap was held at 20 K with *n*-D_2 buffer gas due to its tendency to freeze at lower temperatures. The ion trap was held at 40 K with *p*-H_2 to maximize production of *p*-FH_2^-; at very low temperatures, the equilibrium constants for the formation of the FH_2^- complexes are expected to favor *o*-H_2 over *p*-H_2, counteracting the initial spin isomer enrichment (*33*).

The ions were then transferred to a time-of-flight mass spectrometer and directed to the interaction volume of a VMI electron spectrometer. The VMI was calibrated to the well-characterized detachment transitions of F^- (*25*). We obtain highest resolution at lowest E_{ke} as $\Delta E_{ke} \propto E_{ke}^{1/2}$, but the cross-sections for these systems roughly follow $\sigma \propto E_{ke}^{3/2}$, with a rapidly vanishing signal with increasing resolution (*19*). We obtained overview lower-resolution spectra at high E_{ke} to minimize the effects of near-threshold intensity variations and obtain meaningful relative intensities. We also obtained higher-resolution, lower-E_{ke} spectra in an attempt to resolve possible resonance features. With improved signal-to-noise, we record spectra at photon energies down to ~500–1000 cm^{-1} above all features of interest, with an instrumental resolution of 20–30 cm^{-1} (2.5–3.7 meV) FWHM. This should be compared to the previous report prior to installation of the cryogenic ion trap in which spectra were obtained ~1000–1500 cm^{-1} above the

features of interest, with a resolution of 30–40 cm^{-1} (3.7–5.0 meV) FWHM (*19*) and, more importantly, considerably poorer signal-to-noise.

Image acquisition includes event-counting and centroiding for each photoelectron event (*34*); no photoelectron events are discarded, and even spatially large spots on the image can be reduced to a single point with subpixel resolution. Moreover, as each event is spread over multiple pixels, the effects of pixel noise are minimized. This protocol allows for high-resolution images without sacrificing sensitivity.

The resulting photoelectron images are 2D projections of the full electron velocity distributions. As the linearly polarized detachment laser gives a unique axis of symmetry, the original 3D distribution can be reconstructed in principle. We have found that the MEVELER method (*35*), which relies on maximum entropy methods, reproduces the original distributions from simulated photoelectron images more faithfully, particularly for the difficult case of a weak sharp resonance superimposed on a strong broad signal, as we expect to see for FH_2^- spectra (*17*).

The photoelectron angular distribution (PAD) for all observed features is aligned parallel to the laser polarization axis. There is a near-isotropic unstructured photoelectron signal coming from detachment to the higher-lying repulsive $^2\Pi$ surface *(23)*. Detachment to the $^2\Pi$ nonreactive surface has largely *s*-wave (l=0) character, while detachment to the reactive $^2\Sigma$ surface is largely *p*-wave (l=1); according to the Wigner threshold law for photodetachment (*36*), the cross section is proportional to $E_{ke}^{\,l+1/2}$ and thus the isotropic component contributes more to the photoelectron spectra at low E_{ke}. Earlier reports have roughly separated these two components by only recording the photoelectron signal parallel to the detachment laser (*16, 26, 37*), or by subtracting the perpendicular component of the signal from the parallel component (*19*). The anisotropy of a given photodetachment transition varies with E_{ke} (*38, 39*), and we record spectra at several different photon energies, so there is no clear way to separate the two detachment components for all spectra. We present the spectra integrated over all angles, noting simply that there is a broad isotropic component on all spectra that contributes most at low E_{ke}. Figs. S1 and S2 show experimental spectra of *p*-FH_2^- and *n*-FD_2^- over a wider range of photon energies than are displayed in Figs. 2 and 3.

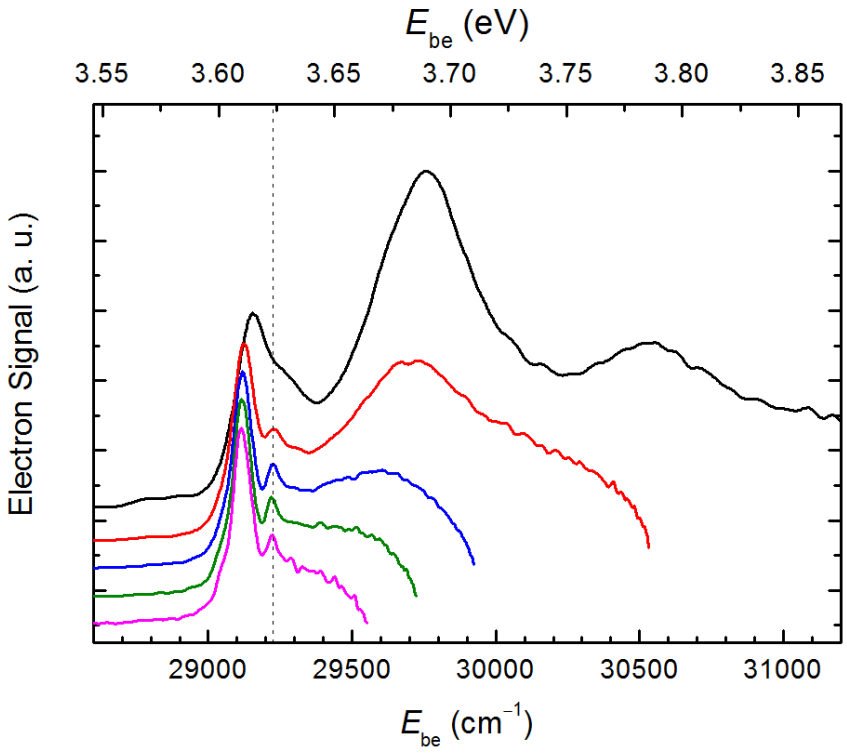

Fig. S1. Experimental SEVI spectra of *p*-FH_2^- over more photon energies than shown in Fig. 2. Spectra are offset vertically for clarity. The weak peak at 29224 cm^{-1} (peak *a* in Fig. 2) is present in several different spectra, but is most evident in the highest-resolution spectra corresponding to the lowest photon energies.

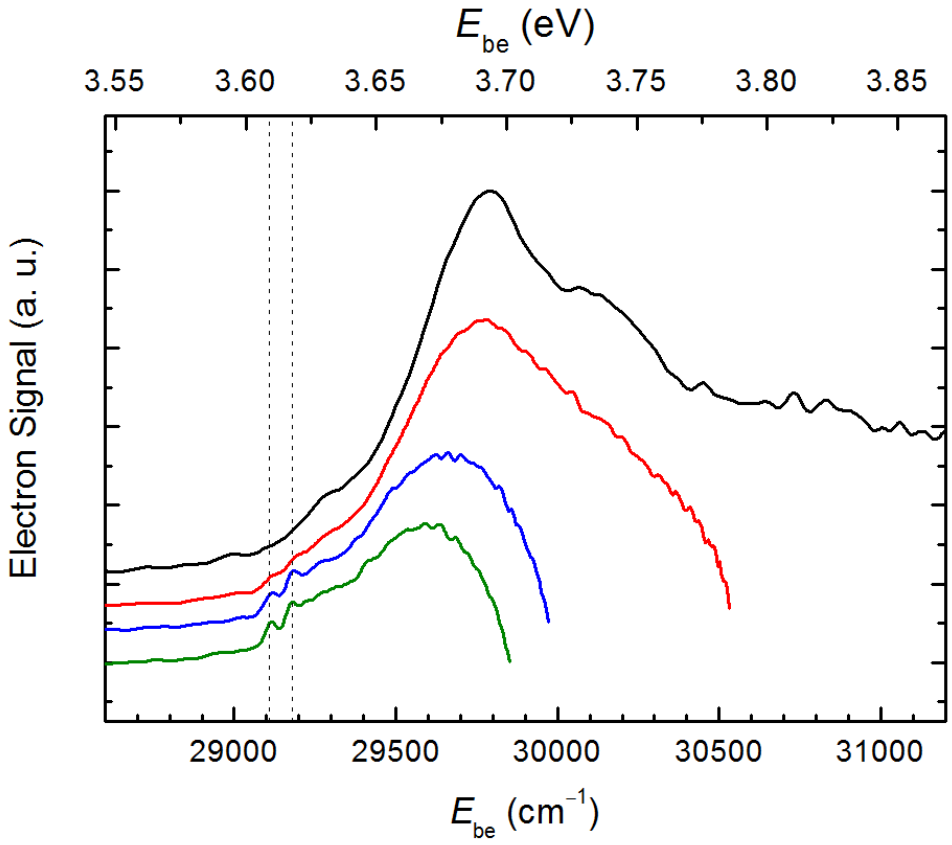

Fig. S2. Experimental SEVI spectra of *n*-FD_2^- over more photon energies than shown in Fig. 3. Spectra are offset vertically for clarity. The weak peaks at 29110 and 29179 cm^{-1} (peaks *b* and *c* in Fig. 3) are present in the higher-resolution spectra.

Theoretical details:

(a) Photodetachment calculations

The present simulations of the *p*-FH_2^- and *n*-FD_2^- photodetachment spectra were performed using the method described by Russell and Manolopoulos (*17*). Under the assumption that the anion is sufficiently rotationally cold to be modeled by total angular momentum $J=0$, and that the electronic dipole matrix element for the bound-continuum electronic transition is a constant function of both the nuclear coordinates in the Franck-Condon region and the energy of the ejected photoelectron, the spectrum $P(E)$ is given by a simple vibrational Franck-Condon factor (*17, 23*)

$$P(E) = \langle \psi | \psi(E) \rangle, \qquad \text{(S1)}$$

where $|\psi\rangle$ is the ground state wave function of the FH_2^- (FD_2^-) anion and

$$\left|\psi(E)\right\rangle = \frac{1}{\pi\hbar}\,\mathrm{Re}\int_0^\infty \exp[-i(H - i\varepsilon - E)t/\hbar]\left|\psi\right\rangle dt \qquad \text{(S2)}$$

Here H is the Hamiltonian of the FH_2 (FD_2) neutral, and ε is a positive infinitesimal that is needed to ensure the convergence of the time integral.

In practice, $|\psi(E)>$ is calculated by propagating the time-dependent wave packet

$$\left|\psi(t)\right\rangle = \exp[-i(H - i\varepsilon)t/\hbar]\left|\psi\right\rangle \qquad \text{(S3)}$$

by means of the symmetric split operator method (*40*). The initial wave function $\left|\psi\right\rangle$ and the neutral Hamiltonian H are both represented in the Jacobi coordinates R, r, γ of the F+H_2 (F+D_2) reactant arrangement, where $R = |\mathbf{R}|$ is the distance from F to the center-of-mass of H_2 (D_2), $r = |\mathbf{r}|$ is the H_2 (D_2) bond length, and γ is the angle between the vectors **R** and **r**. The formal convergence factor $-i\varepsilon$ is replaced in this method by a negative imaginary absorbing potential $V(R,r) = -i\varepsilon(R,r)$ at the edges of the grids in R and r.

In the present calculations we used Colbert-Miller (*41*) sine discrete variable representation grids in $0 < R < 24$ bohr and $0 < r < 24$ bohr, with 205 (278) grid points in R and 107 (152) in r for FH_2 (FD_2). A transmission-free absorbing potential (*42*) was placed on the last half of each of these grids, from 12 to 24 bohr. The angular coordinate γ was discretized using a basis of 151 even Legendre polynomials for *p*-H_2 , 212 even Legendre polynomials for *o*-D_2, and 211 odd Legendre polynomials for *p*-D_2; the *n*-FD_2^- photoelectron spectrum was then calculated as a 2:1 weighted average of the *o*-FD_2^- and *p*-FD_2^- spectra. The time step of the symmetric split operator evolution was 0.11 fs and the wave packet was propagated for 5.76 ps to calculate *P(E)* with 1 meV (Gaussian FWHM) energy resolution. All of these numerical parameters are far better converged than those used by Russell and Manolopoulos in 1996 (*17*).

The key inputs to the photodetachment calculation are the vibrational wave function of the anion and its dissociation energy D_0 (see Eq. (1) in the main text), and the potential energy surface of the neutral FH_2 system. We shall now describe each of these in turn.

(b) FH_2^- wave function and dissociation energy

For the calculations reported in Figs. 2 and 3, we have used the anion wave function of Zhang and Miller (*23*). This is a simple harmonic normal mode approximation to the ground state anion wave function constructed from the equilibrium geometry and harmonic normal mode frequencies obtained in the early *ab initio* calculation of Simons and co-workers (*43*).

For comparison with this simple anion wave function, and in particular to calculate a more accurate dissociation energy D_0 for the anion, we have also performed some new *ab initio* and vibrational bound state calculations on FH_2^-. To determine a 3-dimensional *ab initio* FH_2^- potential energy surface, we chose the explicitly-correlated coupled-cluster method with single, double and non-iterative triple excitations [CCSD(T)-F12a] (*44, 45*) and, in addition, the scaled triples correction (*45*). We used an augmented correlation-consistent triple-zeta basis (aug-cc-pVTZ) with a density-fitting basis (JKFIT) tailored for the F12a calculations (*46-48*).

Calculations, done with the MOLPRO program suite (*49*), were carried out on a grid of 3720 F+H_2 Jacobi coordinates. The interaction energy was calculated in the standard super-molecular approach in which basis set superposition error is removed by computing all the energies with the triatomic basis set:

$$V_{\text{int}}(R,r,\gamma) = E_{\text{FH}_2^-}(R,r,\gamma) - E_{\text{F}^-}(R,r,\gamma) - E_{\text{H}_2}(R,r,\gamma) \qquad \text{(S4)}$$

To determine the vibrational wave function for this anion PES we used a basis consisting of 20 distributed Gaussian functions in R, 10 distributed Gaussian functions in r, and body-frame rotational functions of the H_2 moiety up to j=12 (only even or odd functions depending on the nuclear-spin species).

Table S1 (next page) lists the resulting equilibrium geometry of the anion, its zero-point energy, and the zero-point corrected dissociation energy [$FH_2^-(000) \rightarrow F^- + H_2(v=0, j=0)$]. We compare with values from the earlier calculations of Simons and co-workers (*43*), and those of Stark (*50*), as reported by Hartke and Werner (*51*). In general, for a CCSD(T) calculation, the larger the basis set, the higher the accuracy. The calculations of Simons *et al.* used a triple-zeta basis set, those of Stark were somewhat better than a quadruple zeta basis (*50*). The present calculation, based on the new explicitly correlated (F12) methodology, is comparable to using a fully converged atomic orbital basis.

We see from Table S1 (next page) that our presumably more accurate calculations predict an anion geometry which is slightly more expanded than that of Simons *et al.* (*43*), but almost identical to the earlier calculation of Stark (*50, 51*). The zero-point energy is slightly lower than the estimates based on the harmonic frequencies, as one might expect for a weakly-bound, anharmonic system.

Table S1. Properties of the FH_2^- anion.

Calculation	r_e(FH) *	r_e(HH) *	ε_0 †	D_0 ‡
Simons *et al.*§	3.194	1.455	2990 ‖	0.204
Stark ¶	3.290	1.482	2997 ‖	0.1950
Present	3.302	1.480	2831 #	0.2005 **
				0.2219

* Bond distance in bohr. The minimum corresponds to collinear FHH.
† Zero-point energy in cm^{-1}, with respect to the bottom of the F^-…HH well.
‡ Dissociation energy in eV; $FH_2^-(0,0,0) \rightarrow F^- + H_2(v=0,j=0)$.
§ Ref. (*43*).
‖ Sum of symmetric stretch, antisymmetric stretch and doubly-degenerate bend harmonic zero-point energies: $(\hbar\omega_s + \hbar\omega_a + 2\hbar\omega_b)/2$.
¶ Refs. (*50, 51*) and private communication from H.-J. Werner.
# Energy of the lowest (0,0,0) vibrational level of the anion with respect to the potential minimum.
** The second entry corresponds to FD_2^-.

(c) FH_2 potential energy surface

Several high-quality *ab initio* FH_2 PES's are now available (*24, 31, 52-54*). Here, we used the Li-Werner-Alexander-Lique (LWAL) PES (*24*). Li, Werner, and Alexander described fits to two *ab initio* multi-reference, configuration-interaction calculations, in which the external correlation energy was additionally scaled by factors of 1.05 (LWA-5) and 1.078 (LWA-78). Subsequent, benchmark calculations (*55*) in the region of the barrier showed that the LWA-5 PES gave a better estimate of the barrier height but that the exoergicity (*56*) was predicted better by the LWA-78 PES. The LWAL PES merges the LWA-5 and LWA-78 potentials to allow the best description of both these key properties.

Table S2 (next page) compares some key features of the LWAL PES with those of the early Hartke-Stark-Werner (HSW) surface (*50, 51*), the Werner-Kallay-Gauss (WKG) calculation (*55*), and two recent potential energy surfaces (FXZ and CSZ) from the Dalian group (*31, 54*).

Table S2. Barrier heights and exoergicities of the $F(^2P_{3/2})+H_2$ reaction on various potential energy surfaces.

PES		Exoergicity *	
	E_a / meV †	$\Delta E(0)$ / eV	$\Delta E(3)$ / meV
HSW ‡	83.2	–1.356	51.6
FXZ §	76.8	–1.3885	22.5
CSZ ‖	72.9	–1.3903	20.1
LWAL ¶	71.2	–1.3895	22.2
WKG #	71.3	–1.3875	
experiment		–1.3872 (6) **	22.3 (6) ††

* $F(^2P_{3/2})+ H_2(v=0, j=0) \rightarrow HF(v', j' = 0)+H$, where $v'=0$ and 3.
† Bent barrier height relative to $F(^2P_{3/2})+H_2(r_e)$.
‡ Refs. (*50, 51*).
§ Ref. (*31*).
‖ Ref. (*54*).
¶ Ref. (*24*).
# Ref. (*55*).
** Ref. (*56*).
†† $\Delta E(0)$ from column 3 plus the difference between the experimental v=0 and v=3 HF band origins, taken from http://webbook.nist.gov.

Of the properties considered in this table, the endoergicity $\Delta E(3)$ of the $HF(v'=3,j'=0)+H$ channel relative to $F(^2P_{3/2})+H_2(v=0, j=0)$ is the most relevant to the present problem, as it will have a direct impact on the relative energies of the reactant and product resonances in the photodetachment of p-FH_2^-. Since the FXZ potential of the Dalian group has an endoergicity that is comparable to that of the LWAL surface, and in equally good agreement with the experimental value, we shall compare the predictions of these two surfaces for the photodetachment spectrum of p-FH_2^- below.

(d) Assumption of electronic adiabaticity

In the complete treatment of the scattering of F by H_2, six electronic states are coupled by the electronic and spin-orbit Hamiltonians [see Eqs. (20) and (25) of Ref. (*57*)]. Instead of a single PES, the system is described by four electronic PES's, which we designate V_Σ, V_Π, V_1, and V_2, as well as two spin-orbit coupling terms, which we designate A and B (*57*). Each of these depends on the three internal coordinates. At each value of the coordinates, diagonalization, of

the 6×6 matrix of the full Hamiltonian gives rise to three electronically-adiabatic states, each of which is doubly-degenerate.

In the region where the anion vibrational wave function is localized, two of the three pairs of states lie at much higher energy (*57*). We accordingly assume that after photodetachment of the electron, the neutral FH_2 evolves on a potential energy surface defined by the coordinate-dependent energy of this lowest electronically-adiabatic state. In addition, we ignore the electronic spin (S=1/2) of this state. These assumptions are entirely reasonable for the photodetachment of FH_2^- and FD_2^-. (In the case of ClH_2^-, for which the spin-orbit interaction is stronger and the Franck-Condon region coincides with the van der Waals well in the reactant valley where the electronic states of ClH_2 are closer in energy, a fully non-adiabatic treatment is required to give quantitative agreement with the experimental SEVI spectrum (*58*). Our results here show that this is not necessary for FH_2^-.)

Additional Theoretical Results

(a) Comparison of anion vibrational wave functions

Figure S3 (next page) shows a comparison of the *p*-FH_2^- photodetachment spectra obtained from simulations on the LWAL FH_2 PES with two different choices of the anion vibrational wave function: the Zhang-Miller fit to the earlier calculation of Simons and co-workers and the more sophisticated calculation described above.

We see from Table S1 that our presumably more accurate calculations predict an anion geometry which is slightly more expanded than that of Simons *et al.* (*43*), but almost identical to the earlier calculation of Stark (*50, 51*). The zero-point energy is slightly lower than the estimates based on the harmonic frequencies, as one might expect for a weakly-bound, anharmonic system.

We observe that there is very little difference between the spectra simulated with the two anion wave functions, even at 1 meV resolution (the difference is even less at 3 meV resolution). The calculated photodetachment peak positions are in the same places in both simulations, as they must be because these positions are determined by the dynamics of the FH_2 neutral. The simulation based on the Zhang-Miller vibrational wave function gives a slightly better fit to the experimental spectrum in terms of the relative intensities of peaks α, *A*, *a*, and β (compare also with Fig. 2). This better agreement likely reflects a fortuitous cancellation of errors: Inaccuracies introduced by the Condon approximation, in which we assume a constant electronic

transition moment, are compensated by the use of a less-accurate vibrational wave function for the negative ion.

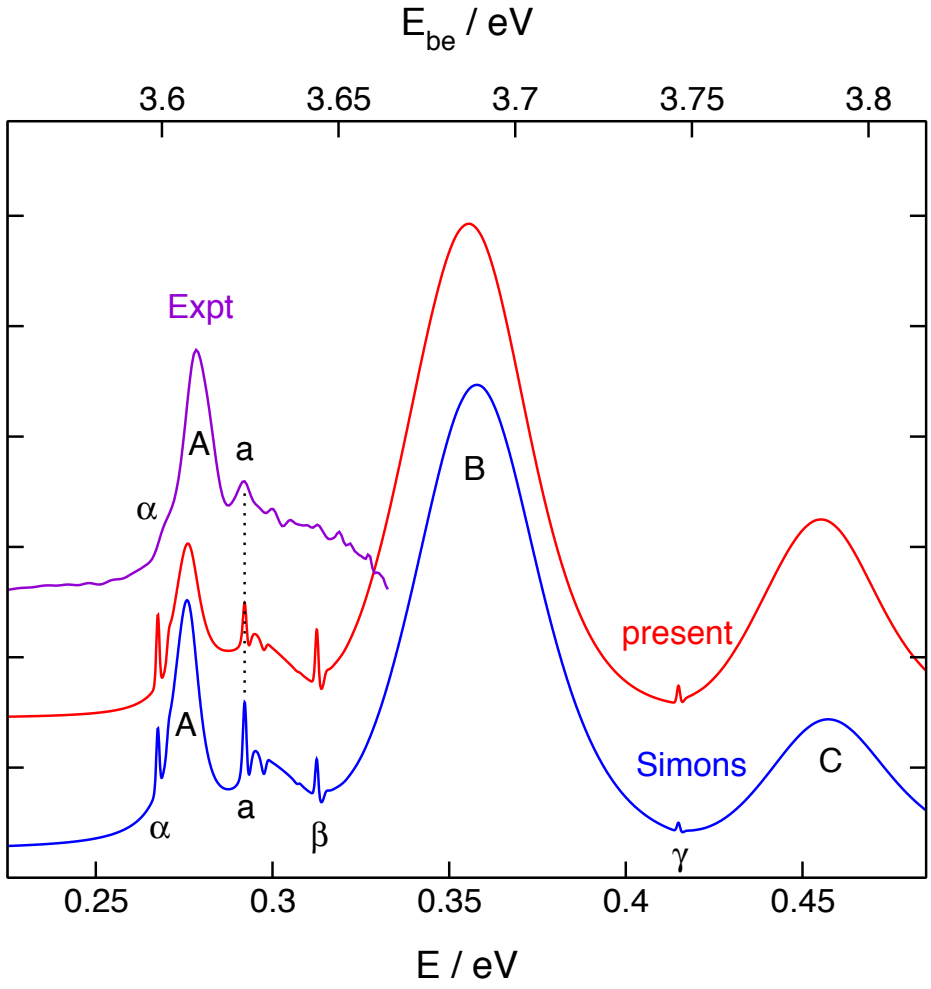

Fig. S3. Photodetachment spectra of *p*-FH_2^-. Purple: highest resolution experimental scan. Red and blue: theoretical simulations at 1 meV energy resolution using the LWAL potential energy surface for the FH_2 neutral and (red) the present anion wave function or (blue) the anion wave function based on the earlier *ab initio* calculations of Simons and coworkers (*43*).

(b) Comparison of neutral potential energy surfaces

Figure S4 (next page) compares the *p*-FH_2^- photodetachment spectra obtained using two recent neutral potential energy surfaces – the LWAL surface of Lique *et al. (24)* and the FXZ surface from the Dalian group (*31*). The Simons anion vibrational wave function was used in both cases.

There is a bigger difference between these results than between the calculations using different anion wave functions in Fig. S3. The reactant resonances α and β are in the same positions on both neutral surfaces, but the product resonance *a* is shifted away from its correct

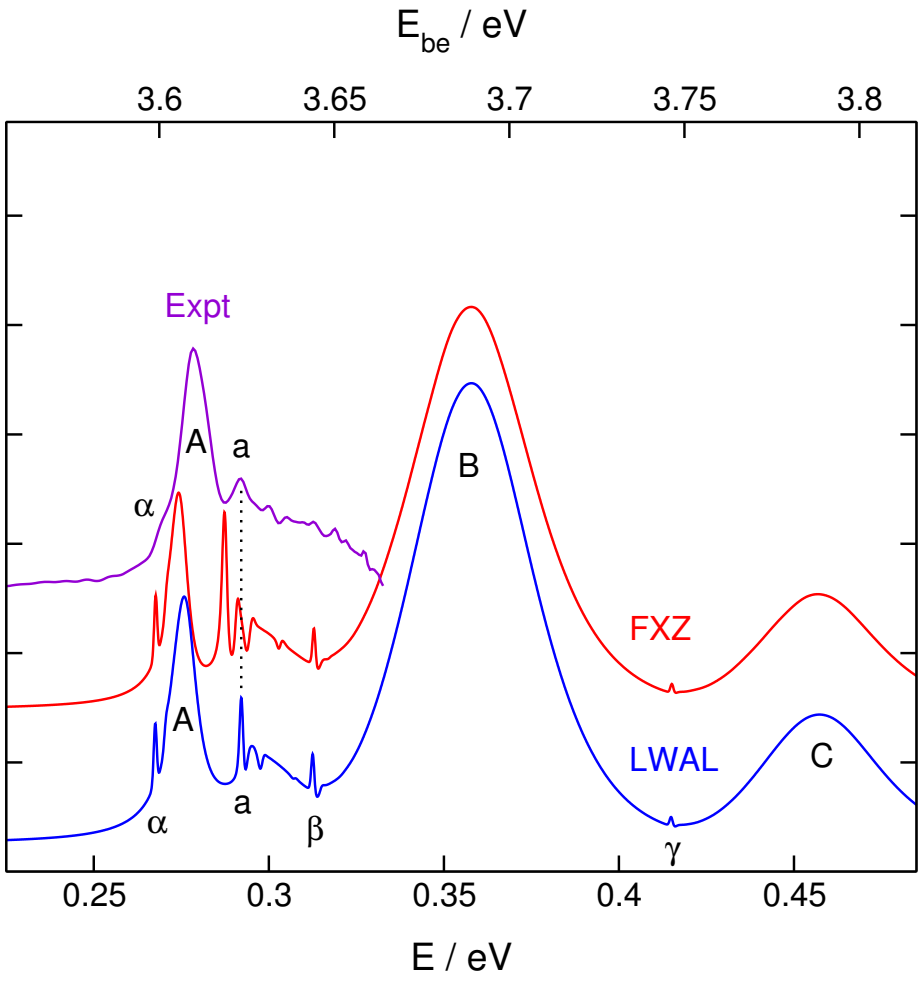

Fig. S4. Photodetachment spectra of *p*-FH_2^-. Purple: highest resolution experimental scan. Red and blue curves: theoretical simulations at 1 meV energy resolution using (blue) the LWAL potential energy surface for the FH_2 neutral (*24*) or (red) the FXZ potential energy surface (*31*). In both cases the Simons anion wave function was used.

position in the calculation on the FXZ surface, worsening the agreement with the high resolution *p*-FH_2^- experiment. This clearly shows that experiment is capable of differentiating between the best available neutral F+H_2 potential energy surfaces. We have chosen the FXZ surface for this comparison because Sun and Zhang have recently argued that it is the best available surface for

accounting for reactive resonances in the F+H_2 and F+HD reactions (*59*). The comparison in Fig. S4 clearly shows that the LWAL surface predicts the position of the product resonance *a* in F+H_2 more accurately than the FXZ surface. Given the assignment of the resonance wave function of peak *a* in Fig. 4, this suggests that, although they predict similar energetic positions of the HF(v′=3,*j*′=0) asymptotes (see Table S2), the LWAL surface provides a more accurate description of the FH_2 potential energy surface in the region of the product van der Waals well.

(c) Quantized bottleneck wave functions

We did not have enough space in the article to give an example of a wave function ψ(*E*) at the energy of a quantized bottleneck. Figure S5 gives two such examples, at the energies of peak *B* in the *p*-FH_2^- spectrum and peak *D* in the *n*-FD_2^- spectrum.

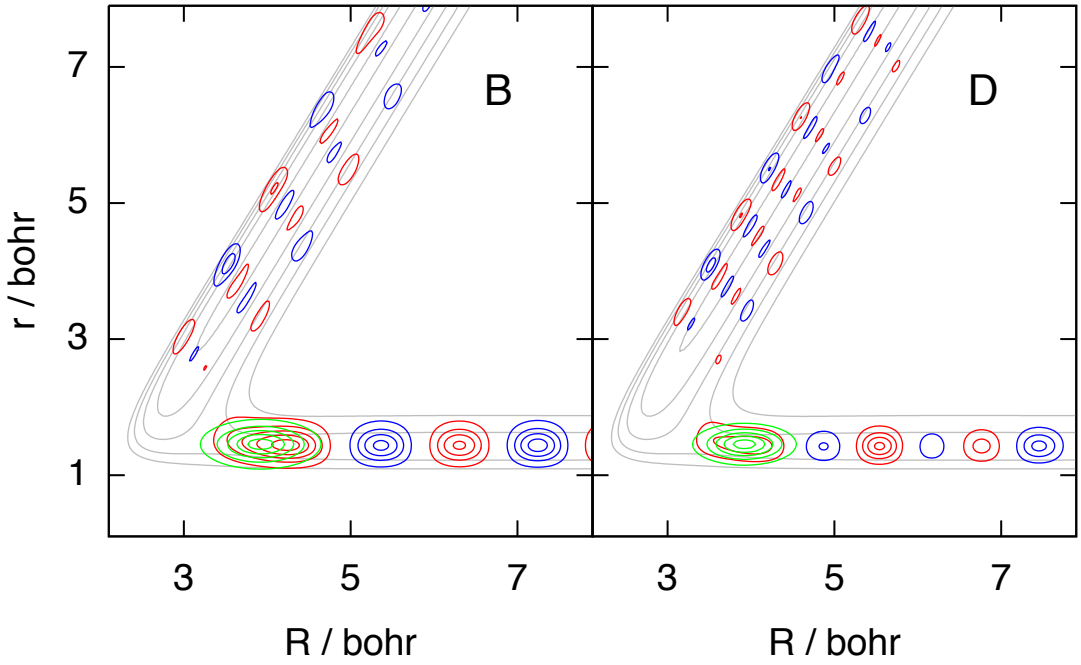

Fig. S5. Quantized bottlenecks: The wave functions ψ(*E*) at the energies of peak *B* in the *p*-FH_2^- spectrum in Fig. 2 and peak *D* in the *n*-FD_2^- spectrum in Fig. 3, plotted in the same way (and with the same contours – which highlight regions of > 10% probability density) as the resonance wave functions in Fig. 4. The contours of the FH_2^- and FD_2^- anion wave functions are again shown in green.

One sees that these quantized bottleneck states are delocalized along the reaction coordinate, and that they therefore have an entirely different structure (and physical origin – the slowing down of the reactants as they approach the top of an adiabatic reaction barrier (*30*)) from

the resonance wave functions in Fig. 4. Both quantized bottleneck states clearly have a good Franck-Condon overlap with their respective anion wave functions, which is why they lead to such pronounced peaks in the photodetachment spectra.

(d) Why there are two product resonances in the n-FD_2^- spectrum

The high resolution experimental photodetachment spectrum of *p*-FH_2^- in Fig. 2 shows just one product resonance peak (*a*), whereas the high resolution spectrum of *n*-FD_2^- in Fig. 3 shows two (*b* and *c*). This has nothing to do with the fact that *n*-FD_2^- is composed of a 2:1 mixture of *o*-FD_2^- and *p*-FD_2^-, because the resonances that give rise to peaks *b* and *c* are localized in the DF+D product region, and therefore occur at the same energy for both nuclear spin species of the reactant. Instead it is simply a reduced mass effect: because D has twice the mass of H, deuteration leads to more quasi-bound states.

This is illustrated in Fig. S6, which shows the adiabatic bending curves (*27-29*) that correlate with the HF(v′=3,*j*′=0)+H and DF(v′=4,*j*′=0)+D channels on the LWAL potential energy surface. The first of these curves has a shallow well in the van der Waals region that supports one bound state (*a*) in the H-HF stretching coordinate, whereas the second has a slightly deeper well that supports two bound states (*b* and *c*) in the D–DF stretching coordinate. The energies of all three of these bound states are within ~2 meV of the energies of the corresponding scattering

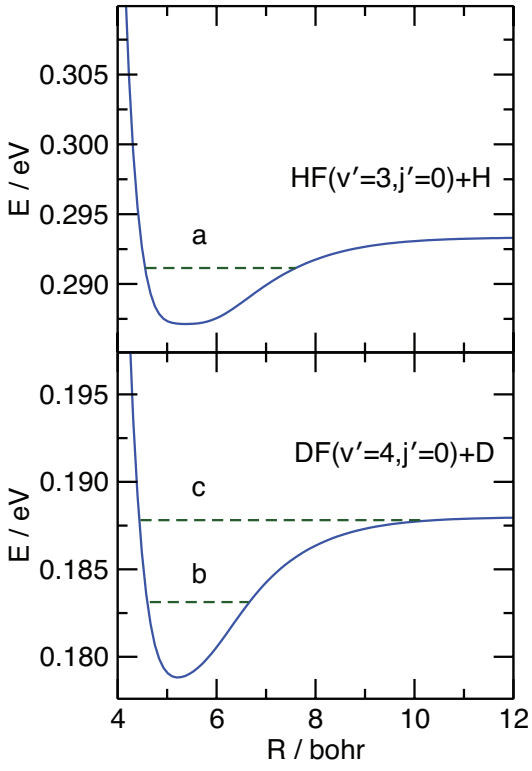

Fig. S6. Adiabatic potential energy curves correlating with the v′=3,*j*′=0 level of HF and the v′=4,*j*′=0 level of DF, as a function of the Jacobi distance *R* from H (D) to the center-of-mass of HF (DF), as calculated on the LWAL potential energy surface. The bound states supported by these curves provide an approximation to the resonances *a*, *b* and *c* seen in the fully coupled calculation.

resonances in Table 1 of the article. In a fully-coupled calculation, the states are quasi-bound because they can decay by vibrational predissociation to HF(v′<3)+H and DF(v′<4)+D product channels, which is not possible within the adiabatic bending approximation.

(e) Contribution of resonances to reactive scattering

The wavefunctions corresponding to the reactant, product and transition state resonances, along with the scattering wavefunctions at the quantized bottlenecks shown in Fig. S5 are localized in the region of the negative ion (shown by the green contours in Figs. 4 and S5) to a slightly greater extent than the unbound (scattering) F+H_2 wavefunction at other energies. This larger overlap gives rise to the peaks in the photodetachment spectra presented in Figs. 2 and 3. These peaks and their intensities are direct spectroscopic manifestations of the elusive resonances associated with the FH_2 potential energy surface. They are not, as we reemphasize here, a measure of the energy dependence of the integral or differential cross sections for the reaction of F with the isotopologues of H_2.

The F+H_2(v,*j*) reaction cross section is given by the following sum of reaction probabilities over all total angular momenta:

$$\sigma_{vj}(E) = \frac{\pi}{(2j+1)k_{vj}^{\,2}} \sum_J (2J+1) P^J{}_{vj}(E) \qquad \text{(S5)}$$

where the reaction probability is a sum over all energetically accessible HF final states (v′*j*′) as well as over all projection quantum numbers of the initial and final rotational angular momenta of the diatomic moiety of the absolute values squared of the corresponding scattering *S*-matrix elements. Here, also, k_{vj} is the wavevector associated with the reactant channel. For the lowest (v=0, *j*=0) state of *p*-H_2, and for *J*=0, the reaction probability predicted by the LWAL PES is shown in Fig. S7 (next page). Superimposed are the positions of the peaks A, a, β, B and C labeled in Fig. 2.

The prominent features in the *p*-FH_2^- photodetachment spectrum contribute in only a minor way to the J=0 reaction probability. In addition, this J=0 probability will make only a small contribution to the overall reaction cross section, because the (2J+1) degeneracy factor in eq. S5 amplifies the importance of higher partial waves. As discussed in the main text, the footprint of resonances in the integral and differential cross sections for the reaction of F with the isotopologues of H_2, particularly HD, have been intensively explored previously. (*9-13*)

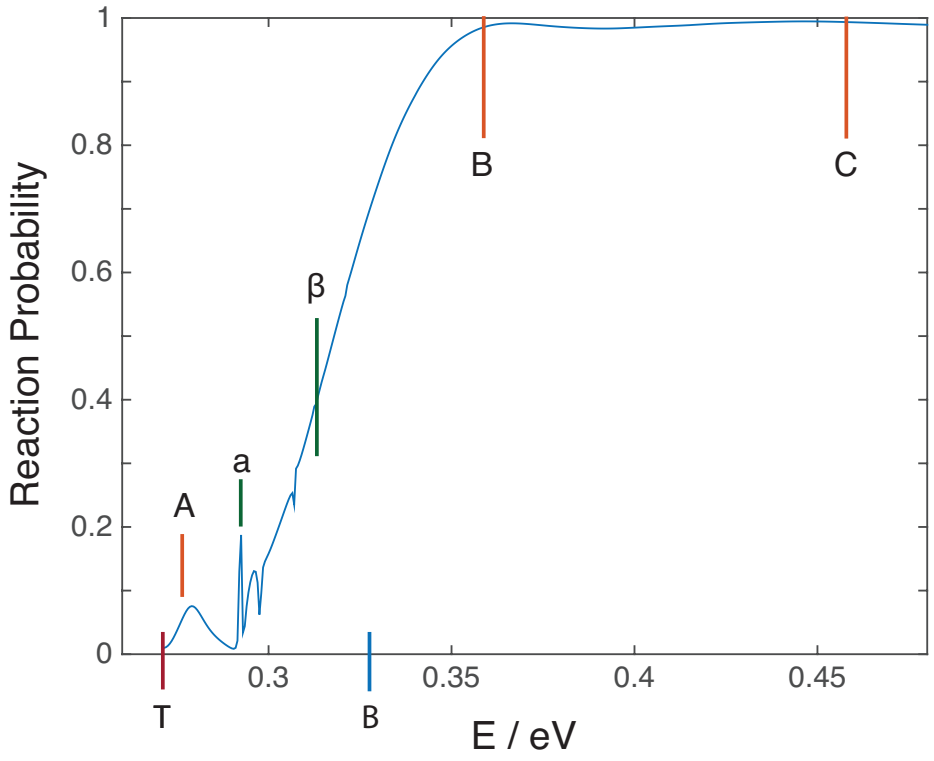

Fig. S7. F+H_2(v=0, j=0)→FH+H J=0 reaction probability as a function of energy as predicted by the LWAL PES. The heavy vertical lines on the abscissa marked "T" and "B" correspond, respectively, to the threshold for reaction (which is the energy of the reactants, with respect of the same zero of energy used in the article) and the energy of the zero-point-corrected barrier to reaction. The positions of the features A, a, β, B and C of Fig. 2 are indicated. The lowest reactant resonance, α, lies *below* the energy of F+H_2(v=0, j=0) and hence is not shown.